

# Temperature dependence of $p$ -wave contacts in a harmonically trapped Fermi gas

Kenta Nagase,<sup>1,\*</sup> Hikaru Takahashi,<sup>1</sup> Soki Oshima,<sup>1</sup> and Takashi Mukaiyama<sup>1,†</sup>

<sup>1</sup>*Department of Physics, Institute of Science Tokyo,  
Ookayama 2-12-1, Meguro-ku, Tokyo 152-8550, Japan*

(Dated: September 8, 2025)

We study the dependence of the  $p$ -wave contact  $C_v$  on the Fermi temperature  $T_F$  and reduced temperature  $T/T_F$  based on the number of closed-channel molecules. From the anisotropic pattern of dissociated molecules, we resolve the narrow  $|m| = 0$  and  $|m| = 1$  dipolar splitting of the  $p$ -wave Feshbach resonance in  $^6\text{Li}$ , enabling the independent determination of the contact for the two components. As  $T_F$  increases, the anisotropy is no longer resolved and the near-resonant contact scales linearly with  $\sqrt{T_F}$ , indicating the contribution of the normalized effective range  $k_F R_e$ . The  $T/T_F$  dependence across the attractive regime reveals opposite trends in the strongly and weakly interacting limits, which are accurately represented by the second-order virial expansion. Our results, together with estimates from the  $p$ -wave virial coefficient, provide a route toward a complete understanding of the thermodynamics of strongly interacting  $p$ -wave Fermi gases.

Understanding pair correlations and their role in fermionic many-body phenomena such as superfluidity is of fundamental importance. Ultracold Fermi gases provide a promising platform to tackle this challenge, owing to the tunability of interactions and thermodynamic quantities. To date, the pair correlations have been quantified by Tan's contact [1–3], which measures short-range correlations between interacting particles and has been extensively characterized in  $s$ -wave systems through various experimental studies [4–6]. These studies have clarified the dependence of the contact on the normalized scattering length  $1/(k_F a)$  and reduced temperature  $T/T_F$ , where  $k_F$  and  $T_F$  denote Fermi wavenumber and temperature, respectively. At unitarity  $a \rightarrow \infty$ , the system exhibits universal behavior solely as a function of  $T/T_F$  [7–11] in both harmonically trapped and homogeneous systems, a hallmark of  $s$ -wave universal thermodynamics. Precise universal thermodynamic measurements at unitarity [12–15], together with temperature-dependent contact studies have considerably deepened our understanding of the equation of state for unitary  $s$ -wave Fermi gases.

Similarly, for systems with  $p$ -wave ( $\ell = 1$ ) interactions, Tan's  $p$ -wave contacts have been theoretically formulated [16–26] and measured experimentally in  $^4\text{K}$  [27–29] and, more recently, in  $^6\text{Li}$  [30]. However, no experiments have yet explored their temperature dependence or performed thermodynamic measurements. The temperature dependence of  $p$ -wave contacts is expected to be more complex than in  $s$ -wave Fermi gases due to the contribution of the effective range. This follows from the effective range expansion of the  $p$ -wave scattering phase shift,  $k \cot \delta_p = -1/(vk^2) - 1/R_e$ , where  $v$  and  $R_e$  are the scattering volume and effective range, respectively [31, 32]. At unitarity  $v \rightarrow \infty$ ,  $v$  dependence vanishes; however, the effective range  $R_e$  scales its scattering. Thus the contacts and thermodynamics cannot be treated universally, as pointed out [30].

Another complication in the temperature dependence

arises from the dipolar splitting of the  $p$ -wave interaction into  $|m| = 0$  and  $|m| = 1$  scattering channels [33, 34]. Especially in  $^6\text{Li}$ , where the Fermi energy  $E_F = k_B T_F$  ( $k_B$ : Boltzmann constant) is comparable to the splitting energy  $\delta E$ , the ratio  $\delta E/E_F$  serves as a key parameter characterizing the system's anisotropy, as noted in early theoretical studies of the  $p$ -wave superfluid phase diagram [35–38] and of  $p$ -wave polarons [39]. To capture the temperature dependence of  $p$ -wave contacts, it is essential to analyze the contributions from each  $m$  channel independently. Besides interaction parameters, a multiple interplay among  $k_B T$ ,  $E_F$ , and  $\delta E$  characterizes the  $p$ -wave contacts. Thus, once the  $E_F$  dependence is established, the  $k_B T/E_F$  dependence can be examined—our main objective in this work.

In this study, we experimentally elucidate how the  $p$ -wave contacts  $C_{v,m}$  ( $m = 0, \pm 1$ ) in a harmonic trap depend on the Fermi temperature  $T_F$  and reduced temperature  $T/T_F$ . The contacts for the  $|m| = 0$  and  $|m| = 1$  components are independently determined from the number and dissociation distribution of closed-channel molecules near the  $p$ -wave Feshbach resonance (pFBR). We find that the two components exhibit quantitatively similar behavior as a function of the normalized dimer energy at all temperatures, while their magnetic-field dependences tend to overlap at higher  $T_F$ . Moreover, near resonance, the contact increases linearly with the normalized effective range  $k_F R_e$ , as  $T_F$  increases. Finally, the  $T/T_F$  dependence of the contacts across the attractive interaction regime is studied, showing opposite trends in the strongly and weakly interacting limits. The excellent agreement with estimates from the second  $p$ -wave virial coefficient demonstrates its utility for describing strongly interacting  $p$ -wave gases and provides key insights for elucidating their equation of state.

The  $p$ -wave contact  $C_{v,m}$  can be defined as the ratio of closed-channel molecules to the total number of atoms when the system is held near a pFBR. The molecular fraction  $f_{c,m}$  in the  $m = 0$  or  $|m| = 1$  channels is given

by [19, 27]

$$f_{c,m} = \ell_{c,m}^{-1} C_{v,m} / 2N, \quad (1)$$

where  $\ell_{c,m} = M\delta\mu_m v_m^{\text{bg}} \Delta B_m / \hbar^2$ . Here,  $M$  is the atomic mass,  $\delta\mu_m$  is the difference in magnetic moment between the closed- and open-channel states, and  $v_m^{\text{bg}} \Delta B_m$  is the product of the background scattering volume and the resonance width. In this study, we exclude the second contact that originates from changes in effective range  $R_e$ . Moreover, assuming the degeneracy of  $m = \pm 1$  channels, we express  $C_{v,|m|=1} = C_{v,m=+1} + C_{v,m=-1}$  as the sum of the  $m = \pm 1$  components.

In the experiment, we prepare spin-polarized  $^6\text{Li}$  atoms in the hyperfine state  $|2\rangle \equiv |F = 1/2, m_F = -1/2\rangle$  in a 1064 nm cigar-shaped optical dipole trap (ODT). The magnetic field is set near 159.1 G, where the pFBR for  $|1\rangle \rightarrow |1\rangle$  ( $|1\rangle \equiv |F = 1/2, m_F = 1/2\rangle$ ) occurs, with a field uncertainty of 2.5 mG. The atom number is fixed at  $N = 1.1(2) \times 10^6$ , while  $T/T_F$  and  $T_F$  are varied to study the temperature dependence.  $T/T_F$  is tuned via the final ODT intensity during evaporative cooling, and  $T_F$  is adjusted by adiabatically ramping up the ODT, keeping  $T/T_F$  constant. With trapping frequencies of  $(\omega_x, \omega_y, \omega_z) = 2\pi \times (660, 9.5, 810)$  Hz at the lowest ODT intensity, we reach  $T/T_F = 0.10(2)$  and  $T_F = 1.5(1) \mu\text{K}$ . For all  $T_F$  values, the ratio of three-axis trapping frequencies is kept constant.

To measure the contact, we quench the  $p$ -wave interaction using a  $6.5 \mu\text{s}$  radio-frequency (rf)  $\pi$ -pulse transferring all atoms from  $|2\rangle$  to  $|1\rangle$ . After a hold time of 0.2–1.5 ms, allowing saturation of the closed-channel fraction, an identical rf-pulse transfers only free atoms back to  $|2\rangle$ ; molecules remain in  $|1\rangle$  because of negligible wavefunction overlap. The molecular fraction is then obtained via state-selective imaging. Because molecules are invisible to imaging light, they are dissociated into atoms by a 1.35 G magnetic-field ramp-up within  $20 \mu\text{s}$ . This rapid ramp-up not only enables molecule detection but also projects their angular momentum distribution onto the absorption image [34, 40–43]. After 1 ms time of flight, the dissociated molecules are imaged at 160.5 G along the  $y$  axis (the ODT beam propagation direction), projecting the  $y$ -integrated distribution onto the  $x$ - $z$  plane with  $z$  aligned to the magnetic field. The number of remaining  $|2\rangle$  atoms is measured at 0 G with an arbitrary time of flight.

Figure 1(a) shows the momentum distribution of dissociated closed-channel molecules at various magnetic-field detunings  $\delta B = B - B_0$ , where  $B_0$  is the resonance field for the  $|m| = 1$  channel. The anisotropy originating from dipolar splitting is evident: with increasing field, the distribution evolves from  $x$ - to  $z$ -oriented, passing through an isotropic, center-hollowed shape. This continuous change reflects a smooth crossover from the  $|m| = 1$  dominated regime to the  $m = 0$  dominated regime via their overlap in the middle.

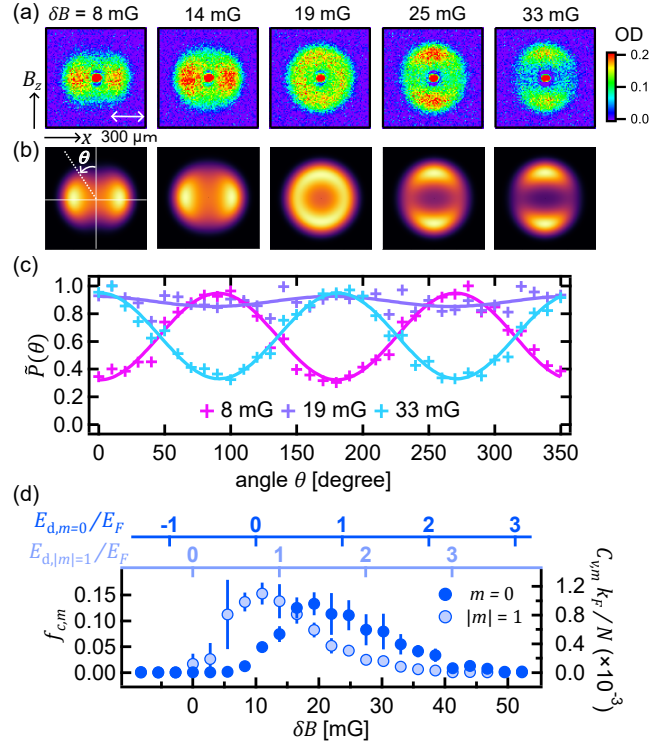


FIG. 1. *Observation of the dipolar splitting.* (a, b) Momentum distributions of dissociated  $p$ -wave closed-channel molecules in the  $x$ - $z$  plane at various magnetic fields: (a) experimental data averaged over 3–6 shots and (b) numerical calculation. The central peaks in (a) originate from open-channel atoms transferred to state  $|2\rangle$ . (c) Normalized angular probability distribution  $\tilde{P}(\theta)$  of dissociated molecules. Fits to Eq. (2) (solid lines) extract the anisotropy parameter  $\gamma$  being 0.99, 0.47, and 0.21 for  $\delta B = 8, 19$ , and  $33$  mG, respectively. (d) Fraction of closed-channel molecules  $f_{c,m}$  and normalized contacts  $C_{v,m} k_F / N$  as functions of magnetic field detuning  $\delta B$  or normalized dimer energy for each  $m$  component. Error bars represent the standard deviations of three repetitions.

To quantify the observed anisotropy, we plot the normalized number of molecules as a function of the polar angle  $\theta$  in the  $x$ - $z$  plane measured from the  $z$  axis ( $0^\circ$ ), as shown in Fig. 1(c). The anisotropy is calibrated as the fraction of  $|m| = 1$  molecules out of total molecules:  $\gamma = N_{c,|m|=1} / (N_{c,m=0} + N_{c,|m|=1})$ . Because dissociated molecules follow the spherical harmonic distribution for  $\ell = 1$ , integrating over the  $y$  axis yields the  $x$ - $z$  distribution [44]

$$\tilde{P}(\theta) = C(\gamma) \left[ \gamma + (1 - 2\gamma) \cdot \frac{2}{3} \cos^2 \theta \right], \quad (2)$$

where  $C(\gamma)$  is a normalization factor. Fitting Fig. 1(c) with Eq. (2) yields  $\gamma$ . Using the obtained  $\gamma$ , we numerically reproduce the dissociated molecular distributions for each image in Fig. 1(b) [44]. The excellent agreement between the experimental and simulated distribu-

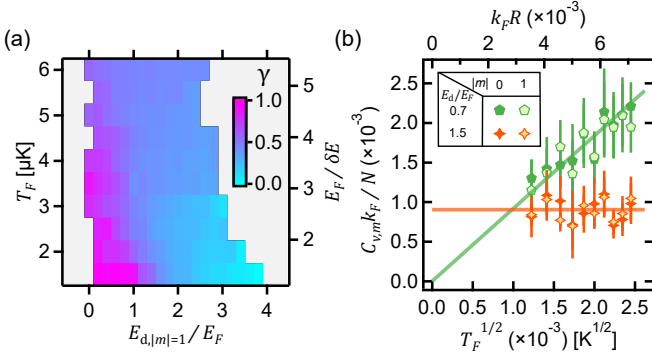


FIG. 2. *Fermi temperature dependence.* (a) Anisotropy parameter  $\gamma$  versus interaction strength (referenced to the  $|m| = 1$  resonance) at various Fermi temperatures  $T_F$ , and inverse normalized splitting energy  $E_F/\delta E$  (right axis). (b)  $C_{v,m}$  versus  $\sqrt{T_F}$  and normalized effective range  $k_F R_e$  in the strong ( $E_{d,m}/E_F = 0.7$ ) and weak (1.5) interaction regimes. Solid lines are guides to the eye.

tions verifies our analysis and successful observation of dipolar splitting.

While the narrow dipolar splitting of the pFBR in  $^6\text{Li}$  has previously been observed in atom-loss spectroscopy in a  $\delta E/E_F \gg 1$  regime by reducing Fermi temperature significantly to the order of 100 nK [40, 45], our measurements combined with a fast  $B$ -sweep can resolve the splitting even at the  $\delta E/E_F \leq 1$  regime with more than one order of magnitude higher  $T_F$ . Remarkably, even at high Fermi temperature of  $T_F = 1.5 \mu\text{K}$ , we see fully polarized  $m = 0$  or  $|m| = 1$  molecules at the corresponding magnetic fields.

Considering the population balance  $\gamma$  in each  $m$  channel, we extract the molecular fraction  $f_{c,m}$  and normalized contact  $C_{v,m} k_F/N$  from Eq. (1) as a function of the magnetic field [Fig. 1(d)]. The molecular fraction  $f_{c,m} = N_{c,m}/N$  is converted to the contact using  $\delta\mu_m = k_B \times 113(7) \mu\text{K}/\text{G}$  [46] and  $v_m^{\text{bg}} \Delta B_m = -2.8(3) \times 10^6 a_0^3$  [47] ( $a_0$ : Bohr radius), assuming both parameters are identical for  $m = 0$  and  $|m| = 1$ . Up to 14(3)% of atoms are converted into molecules in each channel, corresponding to a maximum  $C_{v,m} k_F/N = 1.0(2) \times 10^{-3}$  at  $T/T_F = 0.1$  with  $T_F = 1.5 \mu\text{K}$ . Notably, the  $m = 0$  peak appears at a higher field by 10(2) mG than  $|m| = 1$ , consistent with the result of the atom-loss spectroscopy [45]. To represent this splitting, the top axis in Fig. 1(d) scales the dimer binding energy  $E_{d,m} = -\hbar^2 R_m/(M v_m) = \delta\mu_m \delta B$  [37, 48], with  $R_m = R_e = 11a_0$  [49], normalized by  $E_F$ . In this representation, both  $C_{v,|m|=0}$  and  $C_{v,|m|=1}$  rise sharply near  $E_{d,m}/E_F = 0$  and vanish at  $\approx 2$ , consistent with previous rf spectroscopy and momentum-tail measurements in  $^{40}\text{K}$  [27].

Next, we study the  $T_F$  dependence of the anisotropy and  $p$ -wave contacts while keeping  $T/T_F$  constant. Here,  $T_F$  is varied from 1.5 to 6  $\mu\text{K}$  with  $T/T_F = 0.3(1)$ , thereby changing the normalized splitting energy  $\delta E/E_F$ .

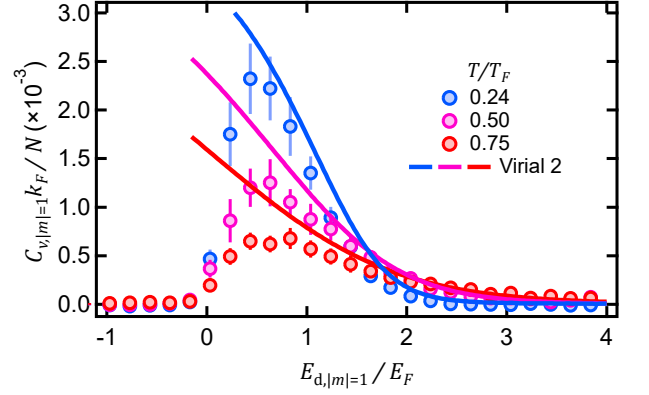


FIG. 3. Dependence of  $p$ -wave contact  $C_{v,|m|=1}$  on interaction strength  $E_{d,|m|=1}/E_F$  at  $T/T_F = 0.24, 0.50$ , and  $0.75$ . The Fermi temperature is fixed at  $T_F = 6.8 \mu\text{K}$  ( $k_F R = 7.6 \times 10^{-3}$ ). The solid lines represent estimates from the second virial coefficient for each  $T/T_F$ . Data for  $C_{v,m=0}$  are omitted because they closely match the  $|m| = 1$  results.

Figure 2(a) shows a 2D map of the population imbalance  $\gamma$  versus  $E_{d,|m|=1}/E_F$  and  $T_F$ . As  $T_F$  increases beyond  $T_F \gtrsim 4.5 \mu\text{K}$  ( $\delta E/E_F \lesssim 0.25$ ), the dissociation distribution becomes nearly isotropic, resulting in  $\gamma \approx 0.5$  for all fields. This is a natural behavior in high  $T_F$  regimes, where  $E_F$  exceeds the splitting energy; thus both channels are resonantly excited simultaneously. Here, we precisely quantify the contribution from both channels for such a crossover regime of interaction symmetry. This will potentially enrich the  $p$ -wave superfluid phase diagram by tuning Fermi temperature.

The Fermi temperature variation also affects the  $p$ -wave contact. Figure 2(b) shows  $C_{v,m}$  versus  $\sqrt{T_F}$  at two representative detunings,  $E_d/E_F = 0.7$  and  $1.5$ . Near resonance ( $E_d/E_F = 0.7$ ), the contact increases linearly with  $\sqrt{T_F}$ , and hence with  $k_F R_e$ . We attribute this to the enhanced role of the effective range near resonance, where the scattering volume diverges and the effective range scales the interaction strength. These observations demonstrate that the  $p$ -wave contacts scale with the dimensionless effective range, as predicted by theoretical models [17, 21]. On the other hand, at  $E_d/E_F = 1.5$ , where the scattering volume dominantly sets the phase shift, the contact is insensitive to  $T_F$ . These results indicate that  $p$ -wave contacts depend on the effective range term near resonance, unlike the  $s$ -wave contacts, and that  $k_F R_e$  normalization is required for universal scaling.

Reflecting the  $T_F$  dependence of the  $p$ -wave contacts, we examine their variation with reduced temperature  $T/T_F$ . Figure 3(a) shows  $C_{v,|m|=1}$  versus interaction strength for various  $T/T_F$  at a fixed  $T_F$ . We find that as the system enters deeper into the degenerate regime, the near-resonant contact ( $E_d/E_F < 1.5$ ) increases, whereas the far-off-resonant contact ( $E_d/E_F > 2$ ) vanishes, yielding a sharper distribution. A distinct feature is observed

at high temperatures; the peak decreases and the contact expands into the far-off-resonant regime. Consequently, the two regimes exhibit opposite temperature dependences.

This feature can be quantitatively described using the quantum virial expansion of the thermodynamic potential in a harmonic trap [50–52]. To account for the anisotropy of the trap, we use the mean trapping frequency  $\omega = (\omega_x \omega_y \omega_z)^{1/3}$ . At high temperatures, the thermodynamic potential of an interacting Fermi gas can be expanded as

$$\Omega = \Omega^{(1)} - k_B T Q_1 [\Delta b_{2,p} z^2 + \Delta b_{3,p} z^3 + \dots], \quad (3)$$

where  $\Omega^{(1)}$  is the non-interacting thermodynamic potential,  $\Delta b_{n,p}$  is the  $n$ th  $p$ -wave virial coefficient, and  $z$  is the fugacity.  $Q_1 = (k_B T / \hbar \omega)^3$  is the single-particle partition function for spinless fermions in a harmonic trap. Applying the adiabatic sweep theorem,  $\delta \Omega / \delta (v^{-1}) = -\hbar^2 C_v / 2M$  [17, 18], and truncating the expansion at second order, we obtain

$$\frac{C_v k_F}{N} = 24\pi (k_F R) \left( \frac{T}{T_F} \right)^3 c_{2,p} z^2, \quad (4)$$

where  $c_{2,p} \equiv \partial \Delta b_{2,p} / \partial (R \lambda^2 / v)$  and  $\lambda \equiv \sqrt{2\pi \hbar^2 / M k_B T}$ . The fugacity  $z$  is determined from the number equation

$$\tilde{\rho} = \tilde{\rho}^{(1)}(z) + 2\Delta b_{2,p} z^2,$$

where  $\tilde{\rho} \equiv (T_F / T)^3 / 6$  and  $\tilde{\rho}^{(1)}(z) \equiv (1/2) \int_0^\infty dt t^2 / (1 + z^{-1} e^t)$  is the non-interacting density in a harmonic trap. To evaluate  $c_{2,p}$ , we use the expression for  $\Delta b_{2,p}$  in an isotropic harmonic trap [53, 54]:

$$\Delta b_{2,p} = \frac{2\ell + 1}{2} \sum_n \left[ e^{-E_{\text{rel},n} / k_B T} - e^{-E_{\text{rel},n}^{(1)} / k_B T} \right], \quad (5)$$

where  $E_{\text{rel},n} = (2\nu_n + 5/2)\hbar\omega$  and  $\nu_n$  satisfies  $\Gamma(-\nu_n) / \Gamma(-\nu_n - 3/2) = -d^3 / 8v - (d/4R)(2\nu_n + 3/2)$  [53, 55], with  $\Gamma$  the gamma function and  $d = \sqrt{2\hbar/M\omega}$  is the characteristic trap length. The non-interacting relative energies are  $E_{\text{rel},n}^{(1)} = (2n + 5/2)\hbar\omega$  ( $n = 0, 1, 2, \dots$ ). We compute  $\Delta b_{2,p}$  and its derivative  $c_{2,p}$  for any interaction strength to illustrate predicted contact in Fig. 3(a) for the experimentally measured temperatures and assume that  $C_{v,m=0} = C_{v,|m|=1} = C_v/2$ .

This estimation, shown as solid lines, clearly captures the reversal of the temperature dependence between the strong and weak interaction regimes, and agrees well with the experimental results in the  $E_d/E_F > 2$  regime. However, as it approaches resonance, the discrepancies become increasingly evident. One reason for this is underestimation of contact due to heating; indeed, we observe a maximum 40% loss in the total atom number accompanied by heating of  $\Delta(T/T_F) \sim +0.2$  near resonance. Another likely reason is the absence of higher-order virial

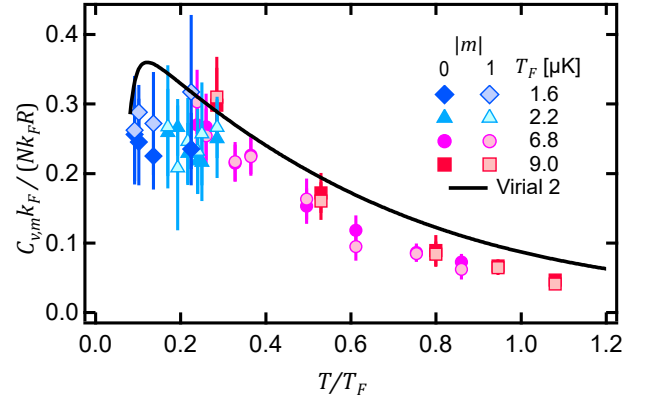


FIG. 4. Peak contact values for  $|m| = 0, 1$  at  $E_d/E_F = 0.7$  normalized by  $k_F R_e$ , as a function of  $T/T_F$ . All data points converge to a single curve by taking  $k_F R_e$  normalization, indicating the universal temperature dependence of the  $p$ -wave contacts. Temperatures are determined before the interaction quench. The black dashed line shows the estimation from the second virial coefficient calculated for  $E_d/E_F = 0.7$ .

coefficients for three- or four-body interactions, which are expected to contribute especially in the strong interaction regime. To explain the contact in the strongly bound regime across unitarity, further theoretical investigation is needed.

Figure 4 shows the contact values measured at  $E_d/E_F = 0.7$  over a wide temperature range. The maximum contact is always observed at this interaction strength regardless of temperature, suggesting another universal feature of  $p$ -wave contacts. To compare data taken at different Fermi temperatures, the contacts are normalized by  $k_F R_e$ , corresponding to the slope of the contact curves in Fig. 2(b) at each  $T/T_F$ . The collapse of the data onto a single trend indicates a universal temperature dependence. Furthermore, the second virial coefficient calculation reproduces the data even deep in the degenerate regime, although it is strictly valid only at high temperatures. This agreement is attributed to the suppression of higher-order virial coefficients in a harmonic trap, which improves the convergence of the expansion [50]. For  $T/T_F \lesssim 0.3$ , the observed contacts appear to saturate or slightly decrease upon further cooling, in qualitative agreement with the Nozières–Schmitt-Rink (NSR) theory [21, 26].

In summary, we have shown that  $p$ -wave contacts  $C_{v,m}$  are governed by both  $T_F$  and  $T/T_F$  due to the presence of dipolar splitting and the effective range contributions, in contrast to  $s$ -wave Fermi gases. Nevertheless, similar to the  $s$ -wave case, the virial expansion provides a powerful framework for estimating thermodynamics. Our results establish a key means for characterizing the many-body properties and thermodynamic behavior of strongly interacting  $p$ -wave Fermi gases.

We acknowledge Shi-Guo Peng for a fruitful discussion

on the second virial coefficient. This work is supported by JSPS KAKENHI Grant Number JP24K00553. The author is supported by the Tsubame Scholarship of Institute of Science Tokyo.

---

\* Contact author: nagase.k.860b@m.isct.ac.jp

† Contact author: mukaiyama@phys.sci.isct.ac.jp

- [1] S. Tan, *Annals of Physics* **323**, 2952 (2008).
- [2] S. Tan, *Annals of Physics* **323**, 2971 (2008).
- [3] S. Tan, *Annals of Physics* **323**, 2987 (2008).
- [4] J. T. Stewart, J. P. Gaebler, T. E. Drake, and D. S. Jin, *Phys. Rev. Lett.* **104**, 235301 (2010).
- [5] G. B. Partridge, K. E. Strecker, R. I. Kamar, M. W. Jack, and R. G. Hulet, *Phys. Rev. Lett.* **95**, 020404 (2005).
- [6] E. D. Kuhnle, H. Hu, X.-J. Liu, P. Dyke, M. Mark, P. D. Drummond, P. Hannaford, and C. J. Vale, *Phys. Rev. Lett.* **105**, 070402 (2010).
- [7] Y. Sagi, T. E. Drake, R. Paudel, and D. S. Jin, *Phys. Rev. Lett.* **109**, 220402 (2012).
- [8] S. Hoinka, M. Lingham, K. Fenech, H. Hu, C. J. Vale, J. E. Drut, and S. Gandolfi, *Phys. Rev. Lett.* **110**, 055305 (2013).
- [9] E. D. Kuhnle, S. Hoinka, P. Dyke, H. Hu, P. Hannaford, and C. J. Vale, *Phys. Rev. Lett.* **106**, 170402 (2011).
- [10] B. Mukherjee, P. B. Patel, Z. Yan, R. J. Fletcher, J. Struck, and M. W. Zwierlein, *Phys. Rev. Lett.* **122**, 203402 (2019).
- [11] K. G. S. Xie, C. J. Dale, K. P. Grehan, M. F. Wang, T. Enss, P. S. Julienne, Z. Yu, and J. H. Thywissen, Dimer-projection contact and the clock shift of a unitary fermi gas (2025), arXiv:2506.13707 [cond-mat.quant-gas].
- [12] S. Nascimbène, N. Navon, K. J. Jiang, F. Chevy, and C. Salomon, *Nature* **463**, 1057 (2010).
- [13] N. Navon, S. Nascimbène, F. Chevy, and C. Salomon, *Science* **328**, 729 (2010).
- [14] M. Horikoshi, S. Nakajima, M. Ueda, and T. Mukaiyama, *Science* **327**, 442 (2010).
- [15] M. J. H. Ku, A. T. Sommer, L. W. Cheuk, and M. W. Zwierlein, *Science* **335**, 563 (2012).
- [16] M. He, S. Zhang, H. M. Chan, and Q. Zhou, *Phys. Rev. Lett.* **116**, 045301 (2016).
- [17] Z. Yu, J. H. Thywissen, and S. Zhang, *Phys. Rev. Lett.* **115**, 135304 (2015).
- [18] Z. Yu, J. H. Thywissen, and S. Zhang, *Phys. Rev. Lett.* **117**, 019901 (2016).
- [19] S. M. Yoshida and M. Ueda, *Phys. Rev. Lett.* **115**, 135303 (2015).
- [20] S.-G. Peng, X.-J. Liu, and H. Hu, *Phys. Rev. A* **94**, 063651 (2016).
- [21] D. Inotani and Y. Ohashi, *Phys. Rev. A* **98**, 023603 (2018).
- [22] F. Qin, X. Cui, and W. Yi, *Phys. Rev. A* **94**, 063616 (2016).
- [23] Y.-C. Zhang and S. Zhang, *Phys. Rev. A* **95**, 023603 (2017).
- [24] X. Yin, X.-W. Guan, Y. Zhang, H. Su, and S. Zhang, *Phys. Rev. A* **98**, 023605 (2018).
- [25] J. Maki, C. J. Dale, J. H. Thywissen, and S. Zhang, *Phys. Rev. A* **110**, 053314 (2024).
- [26] J. Yao and S. Zhang, *Phys. Rev. A* **97**, 043612 (2018).
- [27] C. Luciuk, S. Trotzky, S. Smale, Z. Yu, S. Zhang, and J. H. Thywissen, *Nature Physics* **12**, 599 (2016).
- [28] K. G. Jackson, C. J. Dale, J. Maki, K. G. S. Xie, B. A. Olsen, D. J. M. Ahmed-Braun, S. Zhang, and J. H. Thywissen, *Phys. Rev. X* **13**, 021013 (2023).
- [29] C. J. Dale, K. G. S. Xie, K. Pond Grehan, S. Zhang, J. Maki, and J. H. Thywissen, *Phys. Rev. A* **110**, L051302 (2024).
- [30] K. Nagase, S. Oshima, H. Takahashi, and T. Mukaiyama, *Phys. Rev. A* **111**, 013314 (2025).
- [31] J. R. Taylor, *Scattering Theory: The Quantum Theory of Nonrelativistic Collisions* (Wiley, New York, 1972).
- [32] L. D. Landau and E. M. Lifshitz, *Quantum Mechanics: Non-Relativistic Theory*, Course of Theoretical Physics, Vol. 3 (Butterworth-Heinemann, 1999).
- [33] C. Ticknor, C. A. Regal, D. S. Jin, and J. L. Bohn, *Phys. Rev. A* **69**, 042712 (2004).
- [34] J. P. Gaebler, J. T. Stewart, J. L. Bohn, and D. S. Jin, *Phys. Rev. Lett.* **98**, 200403 (2007).
- [35] M. Iskin and C. A. R. Sá de Melo, *Phys. Rev. Lett.* **96**, 040402 (2006).
- [36] C.-H. Cheng and S.-K. Yip, *Phys. Rev. Lett.* **95**, 070404 (2005).
- [37] V. Gurarie and L. Radzihovsky, *Annals of Physics* **322**, 2 (2007), january Special Issue 2007.
- [38] M. Y. Kagan and D. V. Efremov, *Journal of Experimental and Theoretical Physics* **110**, 426 (2010).
- [39] J. Levinsen, P. Massignan, F. Chevy, and C. Lobo, *Phys. Rev. Lett.* **109**, 075302 (2012).
- [40] S. Peng, S. Peng, L. Ren, S. Liu, B. Liu, J. Li, and L. Luo, Precision measurement of spin-dependent dipolar splitting in  $^6\text{Li}$  p-wave feshbach resonances (2025), arXiv:2505.22409 [cond-mat.quant-gas].
- [41] M. Waseem, Z. Zhang, J. Yoshida, K. Hattori, T. Saito, and T. Mukaiyama, *Journal of Physics B: Atomic, Molecular and Optical Physics* **49**, 204001 (2016).
- [42] T. Volz, S. Dürr, N. Syassen, G. Rempe, E. van Kempen, and S. Kokkelmans, *Phys. Rev. A* **72**, 010704 (2005).
- [43] N. R. Thomas, N. Kjærgaard, P. S. Julienne, and A. C. Wilson, *Phys. Rev. Lett.* **93**, 173201 (2004).
- [44] See Supplemental Material at [URL will be inserted by publisher] for more details.
- [45] M. Gerken, B. Tran, S. Häfner, E. Tiemann, B. Zhu, and M. Weidemüller, *Phys. Rev. A* **100**, 050701 (2019).
- [46] J. Fuchs, C. Ticknor, P. Dyke, G. Veeravalli, E. Kuhnle, W. Rowlands, P. Hannaford, and C. J. Vale, *Phys. Rev. A* **77**, 053616 (2008).
- [47] T. Nakasuji, J. Yoshida, and T. Mukaiyama, *Phys. Rev. A* **88**, 012710 (2013).
- [48] M. Waseem, T. Saito, J. Yoshida, and T. Mukaiyama, *Phys. Rev. A* **96**, 062704 (2017).
- [49] M. Waseem, J. Yoshida, T. Saito, and T. Mukaiyama, *Phys. Rev. A* **98**, 020702 (2018).
- [50] X.-J. Liu, H. Hu, and P. D. Drummond, *Phys. Rev. Lett.* **102**, 160401 (2009).
- [51] H. Hu, X.-J. Liu, and P. D. Drummond, *New Journal of Physics* **13**, 035007 (2011).
- [52] X.-J. Liu, *Physics Reports* **524**, 37 (2013).
- [53] S.-G. Peng, S.-Q. Li, P. D. Drummond, and X.-J. Liu, *Phys. Rev. A* **83**, 063618 (2011).
- [54] C.-X. Zhang, S.-G. Peng, and K. Jiang, *Phys. Rev. A* **98**, 043619 (2018).
- [55] K. Kanjilal and D. Blume, *Phys. Rev. A* **70**, 042709 (2004).



## SUPPLEMENTAL MATERIAL

### ANALYTICAL EXPRESSION FOR THE DISTRIBUTION OF DISSOCIATED $p$ -WAVE MOLECULES

Here, we describe how to extract  $\gamma$ , the fraction of molecules in the  $|m| = 1$  state relative to the total population, from the momentum distribution of dissociated molecules and its angle-dependent profile [Fig. 1(a,c)]. First, we calculate the angular distribution of dissociated atoms that travel a distance  $R$  during the time of flight (TOF). By integrating over the radial distribution  $n(R)$  of the dissociated atoms, we obtain a two-dimensional heat map for a given population balance  $\gamma$ . Figure S1 shows examples of this analysis for  $\gamma = 0$  (left) and  $\gamma = 1$  (right).

#### Angular distribution of dissociated atoms

An abrupt magnetic-field ramp dissociates molecules into atoms with energy  $E_{\text{diss}}$ , which is converted into the kinetic energy of two atoms in opposite directions. During TOF, the atoms travel a distance  $R$  before imaging, and the distribution is projected onto the surface of a sphere of radius  $R$ . From the spherical harmonic functions for the  $p$ -wave case ( $\ell = 1$ ), the probability densities on the sphere are  $\sigma_{m=0} = 3 \cos^2 \Theta / 4\pi$  and  $\sigma_{|m|=1} = 3 \sin^2 \Theta / 4\pi$  for  $m = 0$  and  $|m| = 1$ , respectively, where  $(R, \Theta, \Phi)$  denote the spherical coordinates. The common normalization factor  $3/4\pi$  is omitted in the following discussion.

The on-sphere distribution with probability density  $\sigma$  is projected onto the  $xz$  plane with density  $\sigma^{2D}$  by

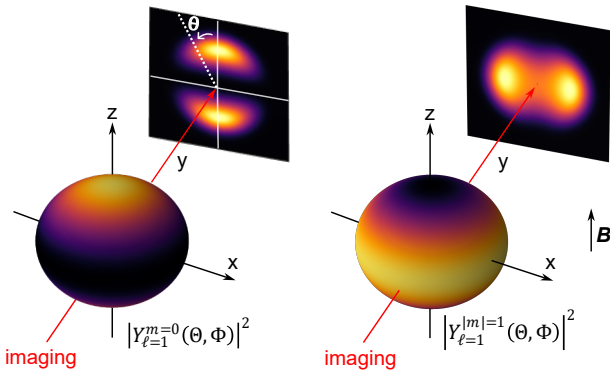


FIG. S1. Schematic of the measurement of the anisotropic distribution of dissociated  $p$ -wave molecules using absorption imaging perpendicular to the magnetic field. The dissociated molecules expand on a sphere with radial distribution  $n(R)$  and angular dependence  $|Y_{\ell}^m(\Theta, \Phi)|^2$  for  $\ell = 1$ . When imaged along the  $y$  axis, the distributions projected onto the  $xz$  plane are  $z$ -weighted for  $m = 0$  and  $x$ -weighted for  $|m| = 1$ .

an imaging beam along the  $y$  axis. Using cylindrical coordinates around the  $y$  axis, the density  $\sigma^{2D}$  at  $(x, z) = (r \sin \theta, r \cos \theta)$ , where  $\theta$  is measured from the  $z$  axis, is given by

$$\sigma_{m=0}^{2D}(r, \theta; R) = \frac{2 \cos^2 \Theta}{\sin \Theta \cos \Phi} = \frac{(r/R)^2}{\sqrt{1 - (r/R)^2}} \cdot 2 \cos^2 \theta, \quad (\text{S1})$$

$$\sigma_{|m|=1}^{2D}(r, \theta; R) = \frac{2 \sin^2 \Theta}{\sin \Theta \cos \Phi} = \frac{2}{\sqrt{1 - (r/R)^2}} - \sigma_{m=0}^{2D}(r, \theta; R). \quad (\text{S2})$$

The prefactor of 2 accounts for the contribution of atoms detected on both the front and back surfaces of the sphere.

The probability density  $P(\theta)$  of finding dissociated atoms within the angular sector  $\theta \sim \theta + d\theta$  in the  $xz$  plane is

$$P_{m=0}(\theta) = \int_0^R r dr \sigma_{m=0}^{2D}(r, \theta; R) = 2R^2 \cdot \frac{2}{3} \cos^2 \theta, \quad (\text{S3})$$

$$P_{|m|=1}(\theta) = \int_0^R r dr \sigma_{|m|=1}^{2D}(r, \theta; R) = 2R^2 \left(1 - \frac{2}{3} \cos^2 \theta\right). \quad (\text{S4})$$

For  $m = 0$ , the atoms are localized near the top and bottom of the  $xz$  plane with vanishing intensity at the center, whereas for  $|m| = 1$ , they are concentrated on the left and right with finite central intensity.

Neglecting the common radial factor  $2R^2$ , we focus on the angular part. Combining the two components with population balance  $\gamma$ , the angular distribution of dissociated atoms is

$$\begin{aligned} P(\theta) &= (1 - \gamma) \cdot \frac{2}{3} \cos^2 \theta + \gamma \cdot \left(1 - \frac{2}{3} \cos^2 \theta\right) \\ &= \gamma + (1 - 2\gamma) \frac{2}{3} \cos^2 \theta. \end{aligned} \quad (\text{S5})$$

For  $\gamma = 0.5$ , corresponding to equal populations in  $m = 0$  and  $|m| = 1$ ,  $P(\theta) = 0.5$  is independent of  $\theta$ , yielding an isotropic 2D scattering pattern, as seen in the middle panels of Fig. 1(a,b).

To fit the peak-normalized angular distribution in Fig. 1(c), we use the function  $A_1 \cos^2 \theta + A_2$ , where  $A_1$  and  $A_2$  are fitting parameters. The population balance  $\gamma$  is related to these parameters as

$$\gamma = \frac{1}{2 + \frac{3}{2}(A_1/A_2)}. \quad (\text{S6})$$

In the main text, the normalized distribution is expressed as  $\tilde{P}(\theta) = C(\gamma)P(\theta)$ , where  $C(\gamma)$  is the normalization factor.

### Computing the 2D heat map of dissociated molecules

The above analysis has been performed for atoms that travel a distance  $R$ . Here we incorporate the radial distribution  $n(R)$  to compute the two-dimensional heat map on the imaging plane. The distribution  $n(R)$  arises from the spread in breakup times of molecules during the magnetic-field ramp. To obtain the observed two-dimensional distribution in absorption imaging, contributions from spheres of different radii must be weighted by  $n(R)$ . The resulting distribution is

$$\int_r^\infty dR n(R) \left[ (1 - \gamma) \sigma_{m=0}^{2D}(r, \theta; R) + \gamma \sigma_{|m|=1}^{2D}(r, \theta; R) \right], \quad (\text{S7})$$

where the integration is restricted to  $r < R < \infty$  so that the square-root terms in Eqs. (S3) and (S4) remain real.

We next derive  $n(R)$  from the dissociation dynamics. During a linear magnetic-field ramp-up, the dissociation energy at time  $t$  is

$$E_{\text{diss}}(t) = \Delta\mu \alpha_B t, \quad (\text{S8})$$

where the ramp begins at  $t = 0$  with rate  $\alpha_B$ , and  $\Delta\mu$  is the magnetic-moment difference between the closed-channel molecular state and the open-channel scattering state of the Feshbach resonance. In our experiment,  $\alpha_B = 67.5$  G/ms and  $\Delta\mu = k_B \times 113(7)$   $\mu\text{K/G}$ .

The number of closed-channel molecules  $N_c(t)$  during the ramp-up decays as

$$\dot{N}_c(t) = -\Gamma(t)N_c(t), \quad (\text{S9})$$

where the dissociation rate  $\Gamma(t)$  is given by [37]

$$\Gamma(t) = A [E_{\text{diss}}(t)]^{3/2} = A(\alpha_B \Delta\mu)^{3/2} t^{3/2}. \quad (\text{S10})$$

Here,  $A = 2\sqrt{m}/(k_e \hbar^2)$ , with  $k_e = 1/R_e$ . Solving Eq. (S9) yields  $N_c(t)$ , and its derivative gives the proportion of molecules dissociated at time  $t$ :

$$\dot{N}_c(t) = -a^2 t^{3/2} \exp\left[-\frac{2a}{5} t^{5/2}\right], \quad (\text{S11})$$

where  $a = A(\alpha_B \Delta\mu)^{3/2}$ .

To obtain the distribution  $n(R)$  of dissociated molecules due to above mechanism, we relate  $R$  to  $t$ :

$$\begin{aligned} \frac{m}{2} \left( \frac{R}{t_{\text{TOF}}} \right)^2 &= E_{\text{diss}}(t) \\ \text{i.e., } t &= \frac{m}{2t_{\text{TOF}}\alpha_B \Delta\mu} R^2 \end{aligned} \quad (\text{S12})$$

Here, we assume that the magnetic field ramp duration (20  $\mu\text{s}$ ) is much shorter than the TOF duration  $t_{\text{TOF}}$  (1 ms), so that all atoms share the same  $t_{\text{TOF}}$ . This assumption breaks down at high temperature or for slow magnetic ramps.

Substituting Eq. (S12) into Eq. (S11) yields  $n(R)$ , normalized as

$$n(R) = \frac{5b^{4/5}}{\Gamma\left(\frac{4}{5}\right)} \cdot R^3 \exp(-bR^5), \quad (\text{S13})$$

where  $b = \frac{2a}{5} \cdot \left( \frac{m}{2t_{\text{TOF}}\alpha_B \Delta\mu} \right)^{5/2}$ . Numerical calculation of Eq. (S7) for obtained  $\gamma$  yields 2D heat map of dissociated molecules, as in Fig. 1(b) and Fig. S1.